

# Mirror-symmetry violation in bound nuclear ground states

<https://doi.org/10.1038/s41586-020-2123-1>

Received: 23 August 2019

Accepted: 22 January 2020

Published online: 1 April 2020



D. E. M. Hoff<sup>1</sup>✉, A. M. Rogers<sup>1</sup>✉, S. M. Wang<sup>2</sup>, P. C. Bender<sup>1</sup>, K. Brandenburg<sup>3</sup>, K. Childers<sup>2,4</sup>, J. A. Clark<sup>5</sup>, A. C. Dombos<sup>2,6,7</sup>, E. R. Doucet<sup>1</sup>, S. Jin<sup>2,7</sup>, R. Lewis<sup>2,4</sup>, S. N. Liddick<sup>2,4</sup>, C. J. Lister<sup>1</sup>, Z. Meisel<sup>3</sup>, C. Morse<sup>1,9</sup>, W. Nazarewicz<sup>6,8</sup>, H. Schatz<sup>2,6,7</sup>, K. Schmidt<sup>2,7,10</sup>, D. Soltesz<sup>3</sup>, S. K. Subedi<sup>3</sup> & S. Waniganeththi<sup>1</sup>

Conservation laws are deeply related to any symmetry present in a physical system<sup>1,2</sup>. Analogously to electrons in atoms exhibiting spin symmetries<sup>3</sup>, it is possible to consider neutrons and protons in the atomic nucleus as projections of a single fermion with an isobaric spin (isospin) of  $t = 1/2$  (ref. <sup>4</sup>). Every nuclear state is thus characterized by a total isobaric spin  $T$  and a projection  $T_z$ —two quantities that are largely conserved in nuclear reactions and decays<sup>5,6</sup>. A mirror symmetry emerges from this isobaric-spin formalism: nuclei with exchanged numbers of neutrons and protons, known as mirror nuclei, should have an identical set of states<sup>7</sup>, including their ground state, labelled by their total angular momentum  $J$  and parity  $\pi$ . Here we report evidence of mirror-symmetry violation in bound nuclear ground states within the mirror partners strontium-73 and bromine-73. We find that a  $J^\pi = 5/2^-$  spin assignment is needed to explain the proton-emission pattern observed from the  $T = 3/2$  isobaric-analogue state in rubidium-73, which is identical to the ground state of strontium-73. Therefore the ground state of strontium-73 must differ from its  $J^\pi = 1/2^-$  mirror bromine-73. This observation offers insights into charge-symmetry-breaking forces acting in atomic nuclei.

Determining the properties and structure of <sup>73</sup>Rb was primarily motivated by the role this nucleus plays in the rapid proton capture process<sup>8</sup> that is thought to drive thermonuclear type-I X-ray bursts<sup>9,10</sup>. Previous attempts to detect <sup>73</sup>Rb directly have not been successful, owing to its very short half-life, which arises as a result of its proton-unbound ground state<sup>11</sup>. In order to characterize the structure of states in <sup>73</sup>Rb, the nucleus was populated via the  $\beta$  decay of the longer-lived <sup>73</sup>Sr, a technique that has proved effective for several other proton-unbound nuclei<sup>12,13</sup>.

The experiment was performed at the National Superconducting Cyclotron Laboratory (NSCL), which provided a mixed beam of radioactive nuclei containing <sup>73</sup>Sr, derived from fragmentation of <sup>92</sup>Mo (see Methods). Each ion was identified (shown in Fig. 1) before passing through a stack of silicon detectors where they were stopped in a double-sided segmented silicon implantation detector to study their subsequent decays. The segments on the front and back of the detector are perpendicular to each other, enabling spatial localization of the implantation event, which considerably reduces the background when searching for decay events. Over the course of the run, 427 <sup>73</sup>Sr implantation events were unambiguously identified. In a given <sup>73</sup>Sr decay event, a positron ( $\beta^+$ ) is emitted first, quickly followed by the emission of a proton. The  $\beta^+$  particles have a continuous energy distribution, and usually leave only a small fraction of their energy in the silicon

detector. However, the emitted proton is stopped and deposits all of its energy into the silicon implantation detector. The summed energy deposited by the  $\beta^+$  particles and protons results in an energy broadening and shift in the charged-particle spectra (referred to as  $\beta$  summing). The implantation detector was surrounded by germanium detectors to measure  $\gamma$ -rays in coincidence with these decay events to connect the de-excitation of the daughter nucleus to proton-emitting states.

The time between the implantation of <sup>73</sup>Sr ions into the silicon detector and the subsequent charged-particle events is presented in Fig. 2a, and the data show good agreement with an exponential decay of one species and a constant random background. The half-life of <sup>73</sup>Sr was determined to be  $t_{1/2} = 23.1 \pm 1.4$  ms (all errors herein are  $1\sigma$ ) from the logarithmic-bin method<sup>14</sup>, providing, to our knowledge, the best direct half-life measurement of <sup>73</sup>Sr so far (see Extended Data Fig. 1 and Methods).

The energy spectrum of <sup>73</sup>Sr  $\beta$ -delayed proton-emission events is shown in Fig. 2b, with the measured background denoted by the shaded blue overlay (see Methods). Two strong peaks are observed. The largest peak—found at  $3.93 \pm 0.012$  MeV—is attributed to protons emitted from the  $T = 3/2$  isobaric-analogue state (IAS) in <sup>73</sup>Rb—referred to as <sup>73</sup>Rb\*(IAS)—which leaves behind <sup>72</sup>Kr in its ground state. Correcting for  $\beta$  summing (see Methods) gives a proton energy of  $3.80 \pm 0.02$  MeV, which is in agreement with the previous direct measurement<sup>15</sup> of

<sup>1</sup>Department of Physics and Applied Physics, University of Massachusetts Lowell, Lowell, MA, USA. <sup>2</sup>National Superconducting Cyclotron Laboratory, Michigan State University, East Lansing, MI, USA. <sup>3</sup>Department of Physics and Astronomy, Ohio University, Athens, OH, USA. <sup>4</sup>Department of Chemistry, Michigan State University, East Lansing, MI, USA. <sup>5</sup>Physics Division, Argonne National Laboratory, Argonne, IL, USA. <sup>6</sup>Department of Physics and Astronomy, Michigan State University, East Lansing, MI, USA. <sup>7</sup>JINA-CEE, Michigan State University, East Lansing, MI, USA. <sup>8</sup>FRIB Laboratory, Michigan State University, East Lansing, MI, USA. <sup>9</sup>Present address: Nuclear Science Division, Lawrence Berkeley National Laboratory, Berkeley, CA, USA. <sup>10</sup>Present address: Institute of Nuclear and Particle Physics, TU Dresden, Dresden, Germany. ✉e-mail: dan@demhoff.com; Andrew\_Rogers@uml.edu

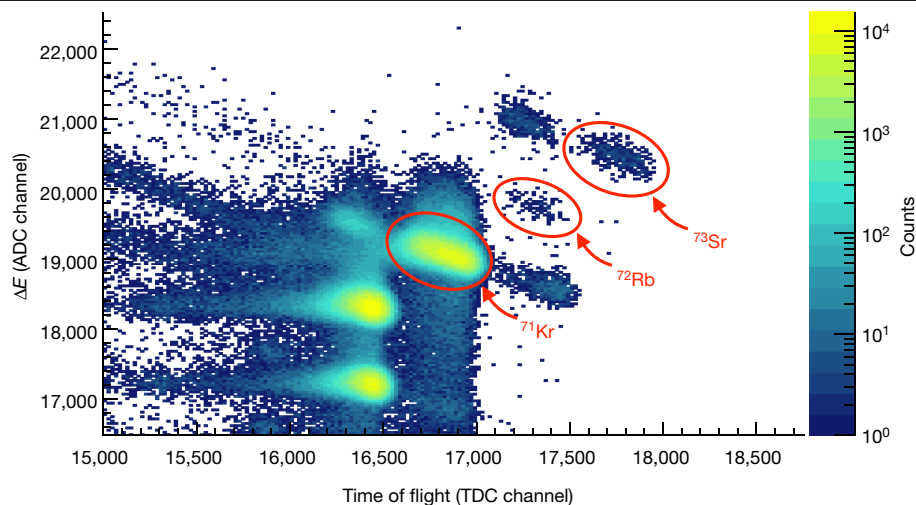


**Fig. 1 | Particle identification plot.** Particle identification was deduced from the energy loss of the incoming heavy ions passing through the first silicon detector in the stack ( $\Delta E$ ) versus the time of flight of the ion after exiting the A1900 fragment separator. The raw uncalibrated signals from the detectors are presented, with the analogue-to-digital converter (ADC) channel for the

relative energy loss on the vertical axis and the recorded time-to-digital converter (TDC) channel on the horizontal axis. The colours represent the total number of counts found. The ion of interest,  $^{73}\text{Sr}$ , is unambiguously isolated from neighbouring ions.

$3.75 \pm 0.04$  MeV. The second strong peak is attributed to the branching of  $^{73}\text{Rb}^*(\text{IAS})$  decays to the  $^{72}\text{Kr}^*(2^+)$  excited state. This is confirmed by the observation of 709-keV  $\gamma$ -rays that are promptly correlated with events in this second proton peak, shown by the inset to Fig. 2b. A peak in the  $\gamma$ -ray spectrum at 511 keV is expected, because two 511-keV  $\gamma$ -rays are emitted in the annihilation of the  $\beta^+$  with electrons. The observation of 10 coincident 709-keV  $\gamma$ -ray events is consistent with almost all protons in this lower-energy peak proceeding to the  $J^\pi = 2^+$  state, and  $<10\%$  to the nearby 671-keV excited  $^{72}\text{Kr}^*(0^+)$  state at the 90% confidence limit.

After accounting for the branching of the proton emission, the  $\beta$ -decay feeding to  $^{73}\text{Rb}^*(\text{IAS})$  was determined to be 63(3)%, as indicated in Fig. 3. This branching ratio, when combined with the predicted  $^{73}\text{Sr}$  mass from the most recent atomic mass evaluations<sup>16</sup>, yields a value of  $\log(ft)$ —a measure of the structural overlap between the initial and final states—of 3.45(6). This value of  $\log(ft)$  is consistent with the conservation of isobaric spin (that is, a  $\Delta T = 0$  superallowed decay) between pure IASs<sup>17</sup>. It should be noted that some isobaric-spin mixing is expected in the  $A = 73$  atomic mass region (enabling  $\Delta T = 1$  transitions) which would reduce the  $\beta$  branching to the IAS<sup>18–20</sup>, but our measurements cannot assess the degree of such mixing.

The branching of  $^{73}\text{Rb}^*(\text{IAS})$  is unusual as compared to similar systems just below the  $A = 73$  mass region. In particular,  $\beta$ -delayed protons from the nuclei  $^{65}\text{Se}$  and  $^{69}\text{Kr}$  predominately populate either the ground state or the excited states of the daughter nucleus<sup>12</sup>, rather than fractionating to the degree observed for  $^{73}\text{Rb}^*(\text{IAS})$ . In the case of  $^{65}\text{Se}$ , which has a  $J^\pi = 3/2^-$  ground state, the resulting decay of  $^{65}\text{As}^*(\text{IAS})$  almost completely proceeds to the  $0^+$  ground state of  $^{64}\text{Ge}$ . The opposite is true for  $^{69}\text{Kr}$ , for which the ground state and the corresponding  $^{69}\text{Br}^*(\text{IAS})$  have  $J^\pi = 5/2^-$ , and thus  $^{69}\text{Br}^*(\text{IAS})$  decays almost exclusively to the first excited  $2^+$  state in  $^{68}\text{Se}$  by emitting a proton that carries away one unit of orbital angular momentum ( $\ell = 1$ ).

For the nuclei involved in the  $\beta$ -delayed proton emission of  $^{73}\text{Sr}$ , the structural situation is more intricate, and thus the standard shell model approach to the wavefunctions is not appropriate<sup>21</sup>. The  $T = 3/2$  mirror-partner nucleus to  $^{73}\text{Sr}$  is  $^{73}\text{Br}$ , which has a highly collective and complex structure; its ground-state spin assignment had been under debate for almost two decades. The rotational band structure of  $^{73}\text{Br}$  suggests that it has a substantial deformation, and a ground state with  $J^\pi = 1/2^-$  that is possibly triaxially shaped<sup>22–26</sup>. Isobaric-spin symmetry would lead us

to expect that  $^{73}\text{Sr}$  should have a similarly highly collective structure, and therefore  $^{73}\text{Rb}^*(\text{IAS})$  as well. The key issue in this discussion is the degree to which strontium and bromine differ.  $^{73}\text{Br}$  has two differently shaped, low-lying collective configurations, separated by only 27 keV, where the ground state has  $J^\pi = 1/2^-$  and the excited configuration has  $J^\pi = 5/2^-$ . It requires only a small degree of charge-symmetry breaking to invert the sequence of these two structures and cause a breakdown of ground-state mirror symmetry. To this extent, the  $A = 73$  isobar is a special case.

To understand the continuum and deformation effects on the open quantum system  $^{73}\text{Rb}^*(\text{IAS})$ , we adopted the Gamow coupled-channel (GCC) approach to model its decay<sup>27,28</sup>. In the framework of GCC, we used the Berggren basis, which is a complete ensemble that includes bound, Gamow and scattering states<sup>21,27,29</sup>. Hence, it provides the correct outgoing asymptotic behaviour to describe the decay of particle-unbound resonances, and in essence enables the treatment of nuclear structure and reactions on the same footing. For this study,  $^{73}\text{Rb}^*(\text{IAS})$  was divided into a deformed core ( $^{72}\text{Kr}$ ) plus a valence proton. The interaction between the deformed  $^{72}\text{Kr}$  core and the valence proton is represented by a Woods–Saxon potential with a quadrupole deformation  $\beta_2$ .

The states in the  $T = 3/2$  quartet along the  $A = 73$  isobar are dominated by prolate deformation, and the daughter nucleus  $^{72}\text{Kr}$  is believed to show strong shape-mixing effects with a predominately oblate-shaped ground state<sup>30–32</sup>. Therefore, the decay of  $^{73}\text{Rb}^*(\text{IAS})$  to the ground-state rotational band of  $^{72}\text{Kr}$  might undergo a transition from a prolate to oblate shape, which would suppress the decay process by reducing the decay width,  $\Gamma_p$ . As no shape-mixing effect can be incorporated into the GCC model, calculations were performed for different deformations and spin assignments of  $^{73}\text{Rb}^*(\text{IAS})$ . The spin assignments were chosen based on the ground-state and first-excited-state spins of  $^{73}\text{Br}$ . The values  $\beta_2 = -0.34$  and  $+0.4$  were chosen for the oblate and prolate shapes, respectively, taken from experimental values for the ground states of  $^{73}\text{Br}$  and  $^{72}\text{Kr}$ <sup>23,25,31</sup>.

On the basis of the predicted branching ratios for  $^{73}\text{Rb}^*(\text{IAS})$  obtained from the GCC calculations, shown in Extended Data Table 1, the only spin assignment consistent with the data is  $J^\pi = 5/2^-$ , when the  $^{72}\text{Kr}$  core is described with oblate-shaped deformation. In this case,  $^{73}\text{Rb}^*(\text{IAS})$  decays to the ground state of  $^{72}\text{Kr}$  through the  $\ell = 3$  channel, and to the first excited  $J^\pi = 2^+$  state through the  $\ell = 3$  and  $\ell = 1$

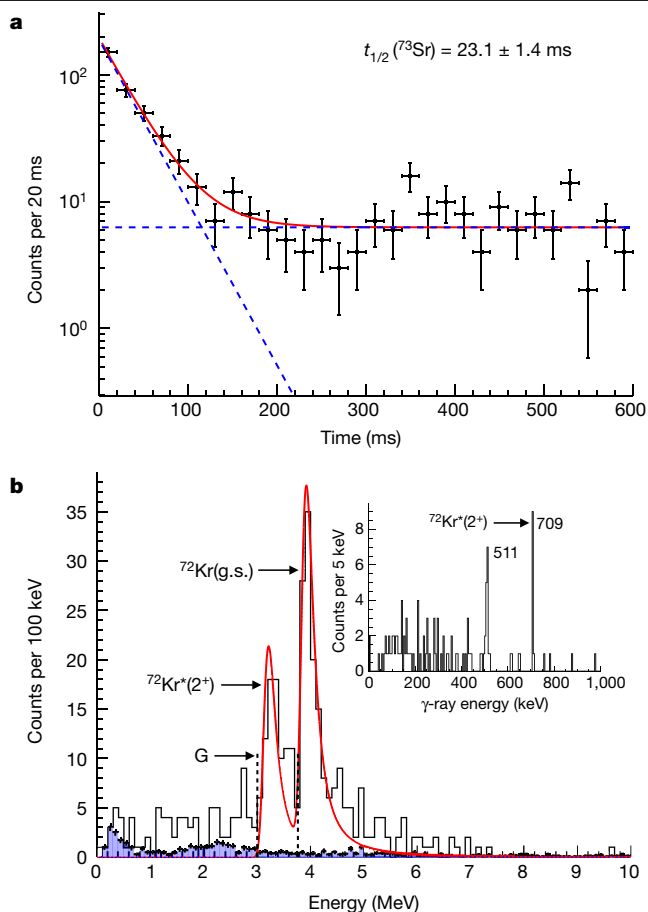


**Fig. 2 | Decay spectra of  $^{73}\text{Sr}$   $\beta$ -delayed proton emission.** **a**, A plot of the correlation time between implantation of  $^{73}\text{Sr}$  ions and their subsequent decay. The solid red curve shows the resulting fit for an exponential with a constant background. The individual components of the fit are shown by the blue dashed lines. The horizontal error bars correspond to the bin size, and the vertical error bars correspond to one standard deviation from counting. **b**, The time-gated ( $t < 200$  ms) energy spectrum of  $\beta + p$  decay events observed after the implantation of  $^{73}\text{Sr}$  ions. The solid red curve is the best fit of the  $^{73}\text{Rb}^*(\text{IAS})$  decay peaks in the spectrum ( $\chi^2_{\text{red}} = 1.5$ ). The inset shows the  $\gamma$ -ray spectrum gated on the lower energy peak by the gate G, highlighting the de-excitation of  $^{72}\text{Kr}^*(2^+)$ . The shaded blue overlay shows the measured background; the horizontal error bars correspond to the bin size and the vertical error bars correspond to one standard deviation from counting. g.s., ground state.

channels. The lower centrifugal barrier of the  $p$ -wave ( $\ell = 1$ ) component compensates for the smaller decay energy of the first excited  $J^\pi = 2^+$  state. Therefore, the decay widths for the ground state and the first excited state are roughly equivalent, even though the configurations of the calculation might be slightly different when considering the effect of shape mixing or changing calculation parameters. The shape-mixing effect is expected to have a similar impact on both transitions; it should roughly cancel out in the branching ratio. Nevertheless, the conclusion that the small admixture of low-angular-momentum components into the wavefunction has a major impact on the decay process is robust and indicates the important role of deformation on the fine structure of decays via proton emission. This feature has been observed before—though not to the same degree—in the proton emitters  $^{131}\text{Eu}$  and  $^{141}\text{Ho}$ <sup>33–36</sup>.

Isobaric spin is clearly not a perfect symmetry considering protons and neutrons have different electric charges<sup>37</sup>, their masses are slightly different (0.14%)<sup>38</sup> and their magnetic moments differ substantially in both magnitude and sign<sup>39</sup>. Moreover, the nuclear force is stronger between neutron–proton ( $np$ ) pairs than between like-nucleon pairs

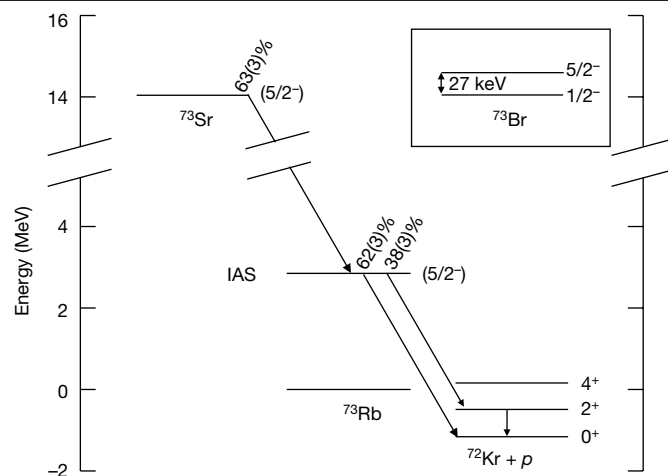


**Fig. 3 | Proposed level scheme.** The level scheme details the  $\beta$ -delayed proton emission of  $^{73}\text{Sr}$  through the IAS in  $^{73}\text{Rb}$ , providing the measured  $\beta$  branching to the IAS and the subsequent proton branching. The ground state and first excited state of  $^{73}\text{Br}$  are given in the inset, contrasted with the ground-state spin assignment of  $^{73}\text{Sr}$ .

( $nn$  and  $pp$ )<sup>40</sup>. With that in mind, it is not at all surprising that nuclear charge-symmetry breaking emerges from the small differences between nucleons and their interactions. Indeed, it is the robust nature of isobaric-spin symmetry that is noteworthy, but those occasions when it breaks down offer a chance to learn more about the forces acting inside the atomic nucleus.

The only other known case of isobaric-spin-symmetry breaking that results in different ground states between mirror nuclei (see Extended Data Fig. 2) is in the  $T = 1$  mirror pair  $^{16}\text{F}/^{16}\text{N}$ , in which  $^{16}\text{F}$  is particle unbound and  $^{16}\text{N}$  is particle bound. This case of isobaric-spin-symmetry breaking is well explained as a consequence of the Coulomb force, in an effect known as the Thomas–Ehrman shift<sup>41–43</sup>. The Thomas–Ehrman shift comes into play for an unbound or loosely bound proton state (the valence proton of  $^{16}\text{F}$ ), because the wavefunction of the proton extends well beyond the surface of the nucleus, resulting in a different asymptotic behaviour than for the bound mirrored neutron (the valence neutron of  $^{16}\text{N}$ ). Such a mechanism is not immediately apparent in the case of  $^{73}\text{Sr}/^{73}\text{Br}$ , and it may be that charge-symmetry-breaking forces need to be incorporated into the nuclear Hamiltonian to fully describe the presented results.

In this Article we report the breakdown of mirror symmetry between the ground states of the particle-bound nuclei  $^{73}\text{Sr}$  and  $^{73}\text{Br}$ , which appear to have  $J^\pi = 5/2^-$  and  $J^\pi = 1/2^-$ , respectively. This difference probably comes about from an inversion of states, which in  $^{73}\text{Br}$  are only 27 keV apart. However, the consequences are appreciable because the  $\beta$  decay is strongly modified. This inversion could be due to small changes in the two competing shapes, particularly their degree of triaxiality, and the coupling to the proton continuum in the IAS of  $^{73}\text{Rb}$ . In fact, in the exotic region of the chart of nuclides near  $^{73}\text{Sr}$ , where the limits of existence for proton-rich nuclei intersect with the  $N = Z$  line, there may be many more instances of mirror-symmetry breaking.

To confirm the findings presented here, the ground-state spin of  $^{73}\text{Sr}$  should be directly measured through  $\beta$ -NMR or similar methods. A direct measurement of the mass of  $^{73}\text{Sr}$  would also be informative in determining the degree to which isobaric-spin symmetry is broken. With existing facilities it will be difficult to make such direct determinations, because the yield of  $^{73}\text{Sr}$  atoms is low; however, as new facilities come on line, studying such exotic nuclei should become possible, enabling continued investigations and a deeper understanding of the cracked isobaric-spin mirror.

## Online content

Any methods, additional references, Nature Research reporting summaries, source data, extended data, supplementary information, acknowledgements, peer review information; details of author contributions and competing interests; and statements of data and code availability are available at <https://doi.org/10.1038/s41586-020-2123-1>.

- Noether, E. Invariant Variationsprobleme. *Nachr. Ges. Wiss. Göttingen Math.-Phys. Kl.* **1918**, 235–257 (1918).
- Elliott, J. & Dawber, P. *Symmetry in Physics: Principles and Simple Applications* (Oxford Univ. Press, 1984).
- Dirac, P. A. M. The quantum theory of the electron. *Proc. R. Soc. Lond. A* **117**, 610–624 (1928).
- Heisenberg, W. On the structure of atomic nuclei. *Z. Phys.* **77**, 1–11 (1932).
- Wigner, E. On the consequences of the symmetry of the nuclear Hamiltonian on the spectroscopy of nuclei. *Phys. Rev.* **51**, 106–119 (1937).
- Wilkinson, D. H. *Isospin in Nuclear Physics* (North Holland Pub. Co., 1970).
- Warner, D., Bentley, M. & Van Isacker, P. The role of isospin symmetry in collective nuclear structure. *Nat. Phys.* **2**, 311–318 (2006).
- Schatz, H. et al. rp-process nucleosynthesis at extreme temperature and density conditions. *Phys. Rep.* **294**, 167–263 (1998).
- Grindlay, J. et al. Discovery of intense X-ray bursts from the globular cluster NGC 6624. *Astrophys. J.* **205**, L127–L130 (1976).
- Woosley, S. E. & Taam, R. E.  $\gamma$ -ray bursts from thermonuclear explosions on neutron stars. *Nature* **263**, 101–103 (1976).
- Suzuki, H. et al. Discovery of  $^{72}\text{Rb}$ : a nuclear sandbank beyond the proton drip line. *Phys. Rev. Lett.* **119**, 192503 (2017).
- Rogers, A. M. et al.  $^{69}\text{Kr}$   $\beta$ -delayed proton emission: a Trojan horse for studying states in proton-unbound  $^{69}\text{Br}$ . *Phys. Rev. C* **84**, 051306 (2011).
- Del Santo, M. et al.  $\beta$ -delayed proton emission of  $^{68}\text{Kr}$  and the  $^{68}\text{Se}$  rp-process waiting point. *Phys. Lett. B* **738**, 453–456 (2014).
- Schmidt, K. H. A new test for random events of an exponential distribution. *Eur. Phys. J. A* **8**, 141–145 (2000).
- Batchelder, J. C. et al. Beta-delayed proton decay of  $^{72}\text{Sr}$ . *Phys. Rev. C* **48**, 2593–2597 (1993).
- Wang, M. et al. The AME2016 atomic mass evaluation: (II). Tables, graphs and references. *Chinese Phys. C* **41**, 030003 (2017).
- Singh, B., Rodriguez, J., Wong, S. & Tuli, J. Review of  $\log ft$  values in  $\beta$  decay. *Nucl. Data Sheets* **84**, 487–563 (1998).
- Hagberg, E. et al. Tests of isospin mixing corrections in superallowed  $0^+ \rightarrow 0^+$   $\beta$  decays. *Phys. Rev. Lett.* **73**, 396–399 (1994).
- Konieczka, M., Baczyk, P. & Satula, W.  $\beta$ -decay study within multireference density functional theory and beyond. *Phys. Rev. C* **93**, 042501 (2016).
- Baczyk, P. et al. Isospin-symmetry breaking in masses of  $N \simeq Z$  nuclei. *Phys. Lett. B* **778**, 178–183 (2018).
- Michel, N., Nazarewicz, W., Płoszajczak, M. & Vertse, T. Shell model in the complex energy plane. *J. Phys. G* **36**, 013101 (2009).
- Murray, G., White, W., Willmott, J. & Entwistle, R. The decay of  $^{79}\text{Br}$ . *Nucl. Phys. A* **142**, 21–34 (1970).
- Wörmann, B. et al. Rotational bands in  $^{79}\text{Br}$ : the disappearance of shape coexistence in  $^{79}\text{Se}$ . *Z. Phys. A* **322**, 171–172 (1985).
- Heese, J. et al. Spectroscopy of high spin states in  $^{79}\text{Br}$ . *Phys. Rev. C* **36**, 2409–2421 (1987).
- Heese, J. et al. Conversion electron and yrast state measurements in  $^{79}\text{Br}$ . *Phys. Rev. C* **41**, 1553–1561 (1990).
- Griffiths, A. G. et al. Magnetic moments and shape coexistence in the light Br isotopes. *Phys. Rev. C* **46**, 2228–2240 (1992).
- Wang, S. M., Michel, N., Nazarewicz, W. & Xu, F. R. Structure and decays of nuclear three-body systems: the Gamow coupled-channel method in Jacobi coordinates. *Phys. Rev. C* **96**, 044307 (2017).
- Wang, S. M. & Nazarewicz, W. Puzzling two-proton decay of  $^{67}\text{Kr}$ . *Phys. Rev. Lett.* **120**, 212502 (2018).
- Berggren, T. On the use of resonant states in eigenfunction expansions of scattering and reaction amplitudes. *Nucl. Phys. A* **109**, 265–287 (1968).
- Bouchez, E. et al. New shape isomer in the self-conjugate nucleus  $^{72}\text{Kr}$ . *Phys. Rev. Lett.* **90**, 082502 (2003).
- Gade, A. et al. Quadrupole deformation of the self-conjugate nucleus  $^{72}\text{Kr}$ . *Phys. Rev. Lett.* **95**, 022502 (2005).
- Iwasaki, H. et al. Evolution of collectivity in  $^{72}\text{Kr}$ : evidence for rapid shape transition. *Phys. Rev. Lett.* **112**, 142502 (2014).
- Rykaczewski, K. et al. Proton emitters  $^{140}\text{Ho}$  and  $^{141}\text{Ho}$ : probing the structure of unbound Nilsson orbitals. *Phys. Rev. C* **60**, 011301 (1999).
- Sonzogni, A. A. et al. Fine structure in the decay of the highly deformed proton emitter  $^{131}\text{Eu}$ . *Phys. Rev. Lett.* **83**, 1116–1118 (1999).
- Kruppa, A. T., Barmore, B., Nazarewicz, W. & Vertse, T. Fine structure in the decay of deformed proton emitters: nonadiabatic approach. *Phys. Rev. Lett.* **84**, 4549–4552 (2000).
- Karny, M. et al. Shell structure beyond the proton drip line studied via proton emission from deformed  $^{141}\text{Ho}$ . *Phys. Lett. B* **664**, 52–56 (2008).
- Miller, G. A., Opper, A. K. & Stephenson, E. J. Charge symmetry breaking and QCD. *Annu. Rev. Nucl. Part. Sci.* **56**, 253–292 (2006).
- Borsanyi, S. et al. Ab initio calculation of the neutron–proton mass difference. *Science* **347**, 1452–1455 (2015).
- Alvarez, L. W. & Bloch, F. A quantitative determination of the neutron moment in absolute nuclear magnetons. *Phys. Rev.* **57**, 111–122 (1940).
- Wiringa, R. B., Stoks, V. G. J. & Schiavilla, R. Accurate nucleon–nucleon potential with charge-independence breaking. *Phys. Rev. C* **51**, 38–51 (1995).
- Thomas, R. G. On the determination of reduced widths from the one-level dispersion formula. *Phys. Rev.* **81**, 148–149 (1951).
- Ehrman, J. B. On the displacement of corresponding energy levels of  $^{13}\text{C}$  and  $^{13}\text{N}$ . *Phys. Rev.* **81**, 412–416 (1951).
- Thomas, R. G. An analysis of the energy levels of the mirror nuclei,  $^{13}\text{C}$  and  $^{13}\text{N}$ . *Phys. Rev.* **88**, 1109–1125 (1952).

**Publisher's note** Springer Nature remains neutral with regard to jurisdictional claims in published maps and institutional affiliations.

© The Author(s), under exclusive licence to Springer Nature Limited 2020

## Methods

### Experimental method

The experiment used a primary  $^{92}\text{Mo}$  beam at an energy of 140 MeV per nucleon, undergoing projectile fragmentation on a  $152.2\text{ mg cm}^{-2}$  beryllium target. Fragmentation products were then passed through the A1900 fragment separator, selecting for  $^{73}\text{Sr}$  (ref. <sup>44</sup>). The secondary  $^{73}\text{Sr}$  beam was further purified by a factor of 4,500 after passing through the Radio Frequency Fragment Separator (RFFS)<sup>45</sup>. The remaining transmitted ions were then sent through a telescope stack<sup>46</sup> consisting of a  $1,041\text{-}\mu\text{m}$  silicon p-i-n detector, a variable-thickness aluminium degrader, a  $989\text{-}\mu\text{m}$  silicon p-i-n detector, a  $520\text{-}\mu\text{m}$  double-sided silicon strip detector (DSSSD) used for implantation, and another  $996\text{-}\mu\text{m}$  single-sided silicon strip detector followed by a plastic scintillator that was used for vetoing ions that were not implanted. The DSSSD was segmented with 40 front and 40 back strips, and the SSSD had 16 strips. The stack was surrounded by a high-purity germanium array—the Segmented Germanium Array (SeGA)—that was used to measure  $\gamma$ -rays<sup>47</sup>.

Nuclei of interest were implanted into the DSSSD detector, allowing for spatial and temporal correlations of implantation and decay events. These heavy ions were identified event-by-event using the measured energy loss in the  $1,041\text{-}\mu\text{m}$  silicon detector at the front of the stack, and the time of flight between the second silicon detector in the stack and a scintillator located at the exit of the focal plane of the A1900. The resulting particle identification spectrum for the region of interest is shown in Fig. 1. Ion identification was confirmed by the observation of known  $\gamma$ -rays in the region of interest.

All of the detector signals were collected using a digital data-acquisition system<sup>48</sup> that used XIA Pixie-16 digitizers, which provided waveforms of the signals as well as timing and pulse-height data. The digitizers had 250-MHz ADCs and 100-MHz clocks that gave 10-ns timestamps. For the presented offline analysis, a  $5\text{-}\mu\text{s}$  gate was used to determine prompt coincidences. The beam rate was about  $6.5(1.3)$  particles per second.

Because the energies associated with the implantation and decay event are several orders of magnitude different (GeV and MeV, respectively), the DSSSD detector was connected to dual-gain preamplifiers. The low-gain setting was used for implantation events and the high-gain setting for decay events. The DSSSD high-gain channels were energy calibrated with  $^{228}\text{Th}$  and  $^{148}\text{Gd}$  sources. SeGA was energy calibrated with a mixed source of well known activity (primarily containing  $^{154}\text{Eu}$ ), that was also used for determining an absolute efficiency curve.

### Experimental analysis

After an ion was tagged by energy-loss and time-of-flight measurements, the ion-implantation event was localized within a pixel defined by the perpendicular front and back strips of the DSSSD with the largest charge deposition. Decay events were searched for within a 5-s correlation window, and only events that were within two neighbouring pixels (for a total of 24 surrounding pixels) of the implantation event were considered. All decay events were rejected if another implantation event occurred within 10 half-lives of the ion of interest,  $^{73}\text{Sr}$ .

### Logarithmic-bin method

The half-life was determined using the logarithmic-bin method, in which the ratio of the bin size to the correlation time ( $\Delta t/t$ ) is constant, which is better suited for low-statistics analysis<sup>14</sup>. The resulting plot is shown in Extended Data Fig. 1, and the maximum logarithmic likelihood fit is given by the solid red curve. Because of the nature of this method, instead of correlating all events within a given time window after the implantation—as was done for analysing the decay energy—only the first event after implantation was considered. Furthermore, the peak position of the probability distribution is directly related to the half-life of the species. Therefore, if other species are present then they will be well separated. Thus in the fit to the peak shown in Extended Data Fig. 1 the events

above  $3 \times 10^8$  ns were not considered. The resulting fit of this distribution ( $\chi^2_{\text{red}} = 1.3$ ) provided a better limit on the half-life of  $^{73}\text{Sr}$ , and so this is the half-life reported and used for the exponential in Fig. 2a. The half-life obtained from directly fitting the data in Fig. 2a is  $t_{1/2} = 23.5 \pm 1.8$  ms.

It should also be noted that the observation of only one species, deduced from Extended Data Fig. 1, suggests that we are only considering ground-state decays of  $^{73}\text{Sr}$ . In the fragmentation process we do expect the population of excited states in the nucleus, and thus a potential low-lying  $J^\pi = 1/2^-$  state may be populated. Such states will predominantly decay by internal conversion (ejecting an orbital electron) and thus be enhanced. Since the ions are fully stripped while in flight, decays via internal conversion will be completely suppressed. However, once the ion is implanted it will recombine with electrons from the detector medium, opening up this decay path. The half-lives for such low-lying excited states—in particular E2 transitions separated by  $\sim 10$  keV—will be  $\sim 1\text{--}100\text{ }\mu\text{s}$ , considering the conversion coefficients for strontium<sup>49</sup> and the Weisskopf estimates of the  $\gamma$ -decay half-lives<sup>50</sup>. These estimates are also consistent with systematic trends in the region<sup>51</sup>. With a deadtime after implantation of  $\sim 5\text{ }\mu\text{s}$  for our measurements, the population of such states will mostly decay to the ground state of  $^{73}\text{Sr}$  before the implantation detector will become sensitive. In any case, if a separate species were present with a half-life greater than our deadtime then it would be observed in Extended Data Fig. 1.

### $\beta$ -summing correction

GEANT4 simulations of the detector configuration, coupled with LISE++ simulations of the implantation depth distribution, suggest that a  $\beta$ -summing correction of  $110 \pm 15$  keV needs to be applied to extract the proton energies<sup>52</sup>. This gives a value of  $Q_{p,\text{measured}} = 3.82$  MeV, where  $Q_{p,\text{measured}}$  is the total measured energy released in the decay, which is split between the proton and the remaining nucleus. However, we also need to include the effect of pulse-height defects in measuring the energy of the recoil nucleus<sup>53</sup>, using  $Q_p = Q_{p,\text{measured}} + (1 - K)Q_p/M$ , where  $K$  is the detection efficiency of the recoil ( $\sim 30\%$  for our case) and  $M$  is the total mass of the decaying system ( $M = 73$  AMU in our case). Applying this correction gives the true value,  $Q_p = 3.85$  MeV. To obtain the value of the emitted protons in the laboratory frame, we also need to account for the recoil energy of the resulting  $^{72}\text{Kr}$ . Thus, the reported energy of the proton is  $E_p = [(M - 1)/M]Q_p$ .

### Fitting the decay-energy spectrum

The background of the decay-energy spectrum—the shaded blue overlay in Fig. 2b—was determined by analysing decay events in the 5-s correlation window that occurred 1 s after implantation. After background subtraction, a  $\chi^2$  minimization of the fit to the decay-energy spectrum was constrained by fitting the largest peak with a Landau distribution (generated by the  $\beta^+$  particle) convoluted with a Gaussian distribution (generated by the proton) of the measured intrinsic detector resolution ( $\sigma = 45$  keV). These shape parameters for the distribution were then fixed, and a second peak with the same shape parameters was added. The energy of the second peak was fixed to be 709 keV lower than original peak. The two peak heights, as well as the energy of the original peak, were then allowed to vary.

From the spectrum shown in Fig. 2b, we do not see a notable number of events above background that are below 1 MeV. Owing to the thickness of our detector and the large value of  $Q_{\beta^+}$  (the total energy released in the  $\beta^+$  decay), we do not expect many, if any,  $\beta^+$  particles to deposit more than 1 MeV into a single (or several) strip(s) of our detector especially when considering the results of our simulation. As such, our data indicate that virtually all  $\beta$ -decay events of  $^{73}\text{Sr}$  are followed by the emission of a proton from  $^{73}\text{Rb}$ .

### Gamow coupled-channel analysis

For this work, the rotational band of the core ( $^{72}\text{Kr}$ ) with  $J \leq J_{\text{core}}^{\text{max}} = 8^+$  is included, of which the core rotational energies were taken from



experiment<sup>54</sup>. The effective core–valence potential has been taken to be a deformed Woods–Saxon form including the spherical spin–orbit term with the ‘universal’ parameter set, which has been successfully applied to nuclei from the  $A \approx 80$  region<sup>55,56</sup>. The Coulomb core–proton potential is calculated assuming that the core charge  $Z_{\text{core}}e$  ( $e$ , unit of electron charge) is uniformly distributed inside the deformed nuclear surface. Since the decay width is very sensitive to the separation energy, in order to have a better description of the decay width, the Woods–Saxon depth  $V_0$  is readjusted to fit the experimental decay energy  $Q_p = 3.85$  MeV. The predicted spectra of  $^{73}\text{Sr}$  and  $^{73}\text{Br}$  using this decay energy and the ‘universal’ parameter set is shown in Extended Data Table 2.

The calculations were carried out in the model space defined by  $\max(\ell) \leq 20$ , where  $\ell$  is the orbital angular momentum between the proton and core. The Berggren basis was used for all channels, and the complex-momentum contour of the Berggren basis is defined by the path  $k = 0 \rightarrow 0.4 \rightarrow 0.2i \rightarrow 0.6 \rightarrow 2 \rightarrow 4 \rightarrow 8 \text{ fm}^{-1}$ , with each segment discretized by 30 points (scattering states).

### Pauli blocking

The supersymmetric transformation method<sup>28,57,58</sup> is a projection technique that can prevent the valence proton from being emitted through already filled orbitals by adding a repulsive core near the origin. For simplicity, spherical orbitals that correspond to the deformed levels occupied in the daughter nucleus are projected out. Hence, to estimate the uncertainty, another calculation was done with the removal of Pauli blocking, which causes the GCC calculations to reduce to solving the coupled-channel Schrödinger equation using nonadiabatic coupling<sup>35</sup>.

To estimate the uncertainty of this projection technique, additional calculations were performed with the removal of Pauli blocking. As a result, the branching to  $^{73}\text{Kr}^*(2^+)$  for the oblate  $J^\pi = 5/2^-$  solution was decreased to 15%, because the  $p_{1/2}$  configuration was considerably reduced (down to 0.02%). However, the presence of a very small  $\ell = 1$  component still allows for a large degree of branching. Therefore, both cases indicate that  $^{73}\text{Rb}^*(\text{IAS})$  has spin and parity  $J^\pi = 5/2^-$ , and thus that  $^{73}\text{Sr}$  has a  $J^\pi = 5/2^-$  ground state, suggesting that the ground and first excited states of  $^{73}\text{Br}$  are inverted relative to its mirror  $^{73}\text{Sr}$ .

### Data availability

Raw data were generated at the National Superconducting Cyclotron Laboratory large-scale facility. All of the relevant data that support the findings of this study are available from the corresponding authors upon reasonable request.

44. Morrissey, D., Sherrill, B., Steiner, M., Stolz, A. & Wiedenhoever, I. Commissioning the A1900 projectile fragment separator. *Nucl. Instrum. Methods Phys. Res. B* **204**, 90–96 (2003).

45. Bazin, D. et al. Radio Frequency Fragment Separator at NSCL. *Nucl. Instrum. Methods Phys. Res. A* **606**, 314–319 (2009).
46. Prisciandaro, J., Morton, A. & Mantica, P. Beta counting system for fast fragmentation beams. *Nucl. Instrum. Methods Phys. Res. A* **505**, 140–143 (2003).
47. Mueller, W. et al. Thirty-two-fold segmented germanium detectors to identify  $\gamma$ -rays from intermediate-energy exotic beams. *Nucl. Instrum. Methods Phys. Res. A* **466**, 492–498 (2001).
48. Prokop, C. et al. Digital data acquisition system implementation at the National Superconducting Cyclotron Laboratory. *Nucl. Instrum. Methods Phys. Res. A* **741**, 163–168 (2014).
49. Kibédi, T., Burrows, T. W., Trzhaskovskaya, M. B., Davidson, P. M. & Nestor, C. W. Jr. Evaluation of theoretical conversion coefficients using Brcc. *Nucl. Instrum. Methods Phys. Res. A* **589**, 202–229 (2008).
50. Condon, E. U. & Odishaw, H. *Handbook of Physics* (McGraw-Hill, 1958).
51. Hagberg, E. et al. The decay of a new nuclide:  $^{73}\text{B}$ . *Nucl. Phys. A* **383**, 109–118 (1982).
52. Meisel, Z. et al.  $\beta$ -particle energy-summing correction for  $\beta$ -delayed proton emission measurements. *Nucl. Instrum. Methods Phys. Res. A* **844**, 45–52 (2017).
53. Huang, W. J. & Audi, G. Corrections of alpha- and proton-decay energies in implantation experiments. *EPJ Web Conf.* **146**, 10007 (2017).
54. International Network of Nuclear Structure and Decay Data Evaluators. Evaluated nuclear structure data file (ENSDF) *National Nuclear Data Center* (Brookhaven National Laboratory, 2020); <https://www.nndc.bnl.gov/ensdf/>.
55. Cwiok, S., Nazarewicz, W., Dudek, J., Skalski, J. & Werner, T. Single-particle energies, wave functions, quadrupole moments and g-factors in an axially deformed Woods–Saxon potential with applications to the two-centre-type nuclear problems. *Comput. Phys. Commun.* **46**, 379–399 (1987).
56. Nazarewicz, W., Dudek, J., Bengtsson, R., Bengtsson, T. & Ragnarsson, I. Microscopic study of the high-spin behaviour in selected  $A \approx 80$  nuclei. *Nucl. Phys. A* **435**, 397–447 (1985).
57. Thompson, I. J. et al. Pauli blocking in three-body models of halo nuclei. *Phys. Rev. C* **61**, 024318 (2000).
58. Thompson, I. J., Nunes, F. M. & Danilin, B. V. FaCE: a tool for three body Faddeev calculations with core excitation. *Comput. Phys. Commun.* **161**, 87–107 (2004); erratum **170**, 296–297 (2005).

**Acknowledgements** We would like to thank T. Ginter for his effort in providing the  $^{73}\text{Sr}$  beam used in the experiment. We acknowledge support from the US DOE, Office of Science, Office of Nuclear Physics under award numbers DE-FG02-94ER40848 (UML), DE-AC02-06CH11357 (ANL), DE-SC0013365 and DE-SC0018083 (FRIB), as well as DE-FG02-88ER40387 and DE-SC0019042 (OU); the NNSA through award numbers DE-NA0003180 (NSSC), DE-NA0000979 (NSSC), DE-NA0003221, DE-NA0003909 and/or DE-NA0002132; and the NSF under contract numbers PHY-1-102511 and PHY 14-30152.

**Author contributions** D.E.M.H. performed the offline analysis and prepared the figures as well as the writing for the manuscript. A.M.R. was the principle investigator of the  $^{73}\text{Sr}$  experiment, was responsible for preparing and executing the measurement with C.M., and aided in writing and preparing the manuscript. S.M.W. performed the GCC calculations, prepared tables and prepared the text for these aspects of the manuscript. C.J.L. and W.N. aided in writing and preparing the manuscript. C.M. led the experimental preparations and oversaw conducting the measurement. S.N.L. assisted in the design, setup, and execution of the experiment. P.C.B., K.B., K.C., J.A.C., A.C.D., E.R.D., S.J., R.L., Z.M., H.S., K.S., D.S. and S.K.S. assisted in setting up the experiment and/or checked the data accumulation online and maintained operation of the experiment. S.W. aided in the offline analysis.

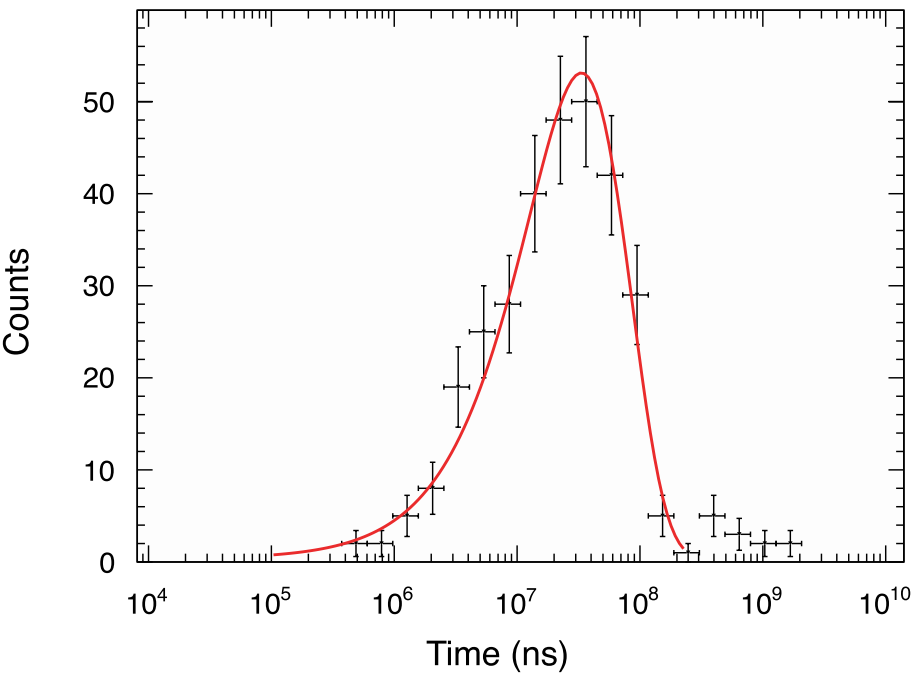
**Competing interests** The authors declare no competing interests.

### Additional information

**Correspondence and requests for materials** should be addressed to D.E.M.H. or A.M.R.

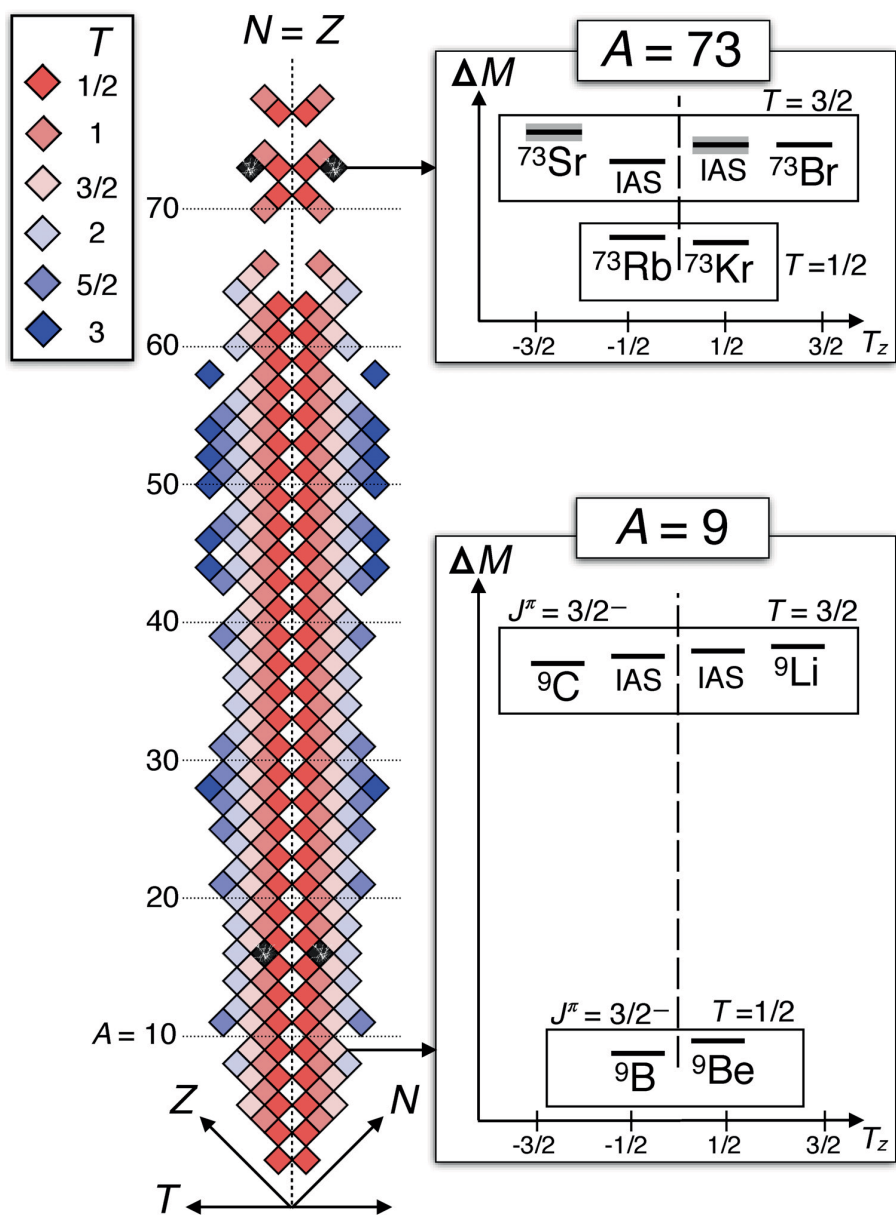
**Peer review information** *Nature* thanks Bertram Blank and the other, anonymous, reviewer(s) for their contribution to the peer review of this work.

**Reprints and permissions information** is available at <http://www.nature.com/reprints>.



**Extended Data Fig. 1 | Time between implantation of  $^{73}\text{Sr}$  and first decay event with logarithmic bins.** The first decay events found after implantation are plotted with logarithmic bins. The resulting maximum logarithmic

likelihood fit to the data is shown as the solid red curve. The horizontal error bars correspond to the bin size, and the vertical error bars correspond to one standard deviation from counting.



**Extended Data Fig. 2 | The mirror chart of nuclides.** Mirror nuclei are plotted according to the isobaric spin ( $T$ ) of their ground-state configurations. For almost the entire mirror chart, the spin and parity,  $J^\pi$ , of the ground states are identically reflected across the  $N=Z$  line<sup>54</sup>. The black squares with cracks show the only two places on the mirror chart where this ground-state mirror symmetry is known or believed to be broken. Once adjusting for the energy

shift of levels due to charge-breaking forces, the relative masses ( $\Delta M$ ) of mirror pairs (with the same magnitude  $T_z$ ) become comparable, and the connection to IASs in neighbouring nuclei becomes clearer. This is illustrated by the isobar diagrams comparing the relative masses for two  $T=3/2$  multiplets, one in the  $A=9$  system and the other in the  $A=73$  system of interest.



Extended Data Table 1 | GCC analysis

Transitions	$\Gamma_p$ (keV)*	Branching	Configurations†
$5/2^- \rightarrow$ g.s. band (oblate)	1.8	49.6% $0^+$ 49.5% $2^+$ 1.1% $4^+$	51.4%( $f_{5/2}, 0^+$ ) 35.0%( $f_{5/2}, 2^+$ ) 6.2%( $p_{1/2}, 2^+$ ) 6.3%( $f_{5/2}, 4^+$ )
$1/2^- \rightarrow$ g.s. band (oblate)	39.8	99.6% $0^+$ 0.4% $2^+$ 0.1% $4^+$	78.8%( $p_{1/2}, 0^+$ ) 19.8%( $f_{5/2}, 2^+$ ) 1.0%( $p_{3/2}, 2^+$ ) 0.4%( $h_{9/2}, 4^+$ )
$5/2^- \rightarrow$ g.s. band (prolate)	7.3	8.2% $0^+$ 90.5% $2^+$ 1.2% $4^+$	23.1%( $f_{5/2}, 0^+$ ) 40.7%( $p_{1/2}, 2^+$ ) 20.2%( $f_{5/2}, 2^+$ ) 10.8%( $f_{5/2}, 4^+$ )
$1/2^- \rightarrow$ g.s. band (prolate)	30.5	98.5% $0^+$ 0.8% $2^+$ 0.6% $4^+$	52.3%( $p_{1/2}, 0^+$ ) 42.8%( $f_{5/2}, 2^+$ ) 2.6%( $p_{3/2}, 2^+$ ) 1.9%( $h_{9/2}, 4^+$ )

The possibilities for the decay of  $^{73}\text{Rb}^*(\text{IAS})$  via proton emission using two different deformations for the  $^{72}\text{Kr}$  core ( $\beta_2 = -0.34$  and  $\beta_2 = 0.4$  for oblate and prolate, respectively) and spin assignments ( $J^\pi = 1/2^-$  or  $5/2^-$ ).

g.s., ground state;  $\Gamma_p$ , decay width.

\*The decay width is inversely related to the half-life of the transition by the Heisenberg uncertainty principle.

†The configurations adopt the spectroscopic notation for angular momentum.

Extended Data Table 2 | Predicted spectra of <sup>73</sup>Sr and <sup>73</sup>Br

Nuclei	oblate ( $\beta_2 = -0.34$ )			prolate ( $\beta_2 = 0.4$ )		
	1/2 <sup>-</sup>	5/2 <sup>-</sup>	$E_x$ (MeV)	1/2 <sup>-</sup>	5/2 <sup>-</sup>	$E_x$ (MeV)
<sup>73</sup> Sr ( $Q_n$ )	-14.945	-15.430	-0.485	-15.219	-15.019	0.200
<sup>73</sup> Br ( $Q_p$ )	-2.927	-3.402	-0.475	-3.139	-2.946	0.193

The core–nucleon interaction is the Woods–Saxon potential with the ‘universal’ parameter. The depth of the Woods–Saxon potential is fitted to the experimental decay energy  $Q_n$  ( $Q_p$ ) for <sup>73</sup>Sr (<sup>73</sup>Br).  
 $E_x$  is the excitation energy of the  $J^\pi = 5/2^-$  state, that is, the energy difference between the two presented states.